

Simulation and modeling of ultrasonic pitch-catch through-tubing logging

Erlend Magnus Viggen¹, Tonni Franke Johansen¹, and Ioan-Alexandru Merciu²

ABSTRACT

Cased petroleum wells must be logged to determine the bonding and hydraulic isolation properties of the sealing material and to determine the structural integrity status. Although ultrasonic pitch-catch logging in single-casing geometries has been widely studied and is commercially available, this is not the case for logging in double-casing geometries despite its increasing importance in plug and abandonment operations. It is therefore important to investigate whether existing logging tools can be used in such geometries. Using a finite-element model of a double-casing geometry with a two-receiver pitch-catch setup, we have simulated through-tubing logging, with fluid between the two casings. We found that there appears a cascade of leaky Lamb wave packets on both casings, linked by leaked wavefronts. By varying the geometry and materials in the model, we have examined the effect on the pulse received from the second wave packet

on the inner casing, sometimes known as the third interface echo. The amplitude of this pulse was found to contain information on the bonded material in the outer annulus. Much stronger amplitude variations were found with two equally thick casings than with a significant thickness difference; relative thickness differences of up to one-third were simulated. Finally, we have developed a simple mathematical model of the wave packets' time evolution to encapsulate and validate our understanding of the wave packet cascade. This model shows a more complex time evolution in the later wave packets than the exponentially attenuated primary packet, which is currently used for single-casing logging. This indicates that tools with more than two receivers, which could measure wave packets' amplitude at more than two points along their time evolution, would be able to draw more information from these later packets. The model was validated against simulations, finding good agreement when the underlying assumptions of the model were satisfied.

INTRODUCTION

In plug and abandonment (P&A) operations, a bore well is hydraulically sealed to prevent leakage from the well structure to the ground surface or to underground geologic formations in an eternal perspective. As the production life of more and more oil fields is coming to an end, the number of upcoming P&A operations is quickly increasing, and expenditures in time and cost are thus set to increase dramatically. It is therefore essential to look into more efficient P&A procedures that still maintain safety.

The planning of P&A operations is based on an evaluation of the well's hydraulic barriers at the time of the operation, and logging-based information has a central role in this evaluation. Cement bond logs may be available, but these may be outdated by several decades, and they may have been performed during well construction with only a single casing present. In most cases, therefore, new logs must be made.

However, existing methods for analyzing log data were typically developed for single-casing geometries, in particular, to evaluate the interface between the casing and the outside material. To use such methods in, e.g., double-casing geometries as shown to the left in Figure 1, the inner casings must be removed to gain access to the outer pipe so that logs can be performed and analyzed. Instead of having to perform this time-consuming and costly process, it would be much preferable to have a method that allows logging through multiple casings, so that most of the pipes can be left in place.

Unfortunately, little has been published on such multiple-casing logging. To achieve these objectives, new techniques must therefore

ades, and they may have been performed during well construction with only a single casing present. In most cases, therefore, new logs must be made.

Manuscript received by the Editor 29 April 2015; revised manuscript received 17 February 2016; published online 27 May 2016; Pagination corrected on 9 June 2016.

¹SINTEF ICT, Acoustics Research Centre, Trondheim, Norway. E-mail: erlendmagnus.viggen@sintef.no; tonni.f.johansen@sintef.no.

²Statoil ASA, Research and Technology, Rotvoll, Norway. E-mail: IOM@statoil.com.

© 2016 Society of Exploration Geophysicists. All rights reserved.

be developed for logging behind multiple casings with sufficient accuracy and azimuthal resolution to provide information on the hydraulic isolation as specified by, e.g., the [NORSOK D-010 \(2013\)](#) standard. For this reason, we are researching the capabilities of current logging technologies in this respect. In doing this, we will start with the simplest case possible before moving to more complex cases; if a given technology does not show potential even for simple cases, there is little point in proceeding with more complex and realistic cases.

Using the terminology of [NORSOK D-010 \(2013\)](#) and referring to Figure 1, this simplest case is evaluating the bonding between the second (i.e., outer) casing and the material in the B-annulus, with fluid in the inner pipe and in the A-annulus. For simplicity, we call this through-tubing logging in this paper.

A variety of logging systems exists using various physical fields to measure cased-hole and multiple-casing corrosion, the most well-known of these being electromagnetic logging systems ([Brill et al., 2011](#); [Arbuzov, 2012](#)). However, our interest is restricted to ultrasonic and sonic logging systems, as their logs are resolved azimuthally and their logging measurements show clear interactions from regular third interfaces. This makes interpretation more difficult because the current ultrasonic and sonic technologies do not provide sufficient information about hydraulic isolation, and they will need to be combined with other measurements to more fully evaluate the hydraulic sealing ([Donovan et al., 2015](#)). In other words, the final log interpretation must involve a complex integration of measured data, well historical information, and experience.

Because of the requirement of [NORSOK D-010 \(2013\)](#) on high-resolution azimuthal mapping, our interest lies in ultrasonic technologies, which have been used for decades in the oil and gas industry for well integrity evaluation of single-cased holes. The technologies are divided into two main types: pulse-echo techniques in which one transducer acts as a transmitter and receiver — see e.g., [Hayman et al. \(1991\)](#) and [Wright \(1993\)](#) — and pitch-catch techniques in which there is one transmitting transducer and one or more receiving transducers, as described by [Zeroug \(2002\)](#), [Zeroug and Froelich \(2003\)](#), [van Kuijk et al. \(2005\)](#), and [van Kuijk et al. \(2006\)](#). A recent review of such ultrasonic techniques is provided by [Wang et al. \(2014\)](#).

In this paper, we examine ultrasonic pitch-catch techniques in which an ultrasonic pulse is emitted from a transmitting transducer toward the casing at an oblique angle. This pulse generates a leaky flexural Lamb wave packet on the pipe (specifically, the A0 Lamb mode). As this wave propagates along the pipe, it leaks a continuous pressure wavefront into the interior and the A-annulus. The wave packet decreases exponentially in amplitude because of this leakage

into the interior and the A-annulus. The amplitude at each point along the emitted pressure wavefront is connected to the amplitude of the Lamb wave packet at the time of emission of the wavefront point. Therefore, the emitted wavefront also decreases exponentially in amplitude, correspondingly to the wave packet. Thus, if we have two receivers R_1 and R_2 placed as shown to the right in Figure 1, the received pressure pulse amplitudes $S_{R_1,1}$ and $S_{R_2,1}$ indicate the Lamb wave packet's attenuation in dB per unit length as

$$\alpha_1 = \frac{20}{\Delta z} \log_{10} \left(\frac{S_{R_1,1}}{S_{R_2,1}} \right), \quad (1)$$

where Δz is the distance between the two receivers.

The attenuation α_1 is determined by the impedance of the materials adjacent to the pipe, as stated by [van Kuijk et al. \(2006\)](#) and shown by [van Kuijk et al. \(2005\)](#) for the case of a plate with material on one side and vacuum on the other side. In a single-casing logging, the measured α_1 can thus be used to find the impedance of the bonded material in the A-annulus.

This Lamb wave packet, henceforth called the primary Lamb wave packet, also leaks a wavefront into the A-annulus. The leaked wave interacts with the outer interface of the A-annulus, causing a reflected wave that generates a secondary Lamb wave packet (A0 mode) on the inner casing, also sometimes called a third interface echo (TIE) by [van Kuijk et al. \(2005\)](#). The arrival time of this wave packet can be used to determine the position of the outer interface, as shown by [Zeroug and Froelich \(2003\)](#) and [van Kuijk et al. \(2005\)](#), and it has been shown by [He et al. \(2014\)](#) that its amplitude is affected by debonding in the A-annulus.

In this paper, we analyze further effects of changes beyond the A-annulus on the wave leaked from the secondary wave packet. As done by [Zeroug and Froelich \(2003\)](#) and [He et al. \(2014\)](#), we simplify the geometry by modeling its 2D sagittal cross section. The analysis uses the signals from the two simulated pitch-catch receivers in the double-casing geometry, meaning that the effects demonstrated in this analysis should also be detectable in a similar physical transducer setup. Thus, this work can be seen as an examination of the untapped potential of existing two-receiver ultrasonic pitch-catch tools, described by [van Kuijk et al. \(2005\)](#) and [Bellabarba et al. \(2008\)](#).

In the following, we will first describe the simulation setup and show and discuss the results. Some of the insights gleaned from this discussion will then be encapsulated into a limited mathematical model of the physical system, which is then validated against simulations.

SIMULATION SETUP

The simulated double-casing geometry is shown to the right in Figure 1. The outer diameter of pipe 1 was chosen as $2a_2 = 7$ in., and its thickness was $a_2 - a_1 = 0.408$ in. For pipe 2, its outer diameter was $2a_4 = 9\frac{5}{8}$ in., and its thickness was $a_4 - a_3 = 0.545$ in. The borehole diameter was $2a_5 = 12\frac{3}{4}$ in. The parameters of the steel and sandstone materials used for the pipes and the formation, respectively, are given in Table A-1. Unless otherwise specified, the two annuli and the interior contained water.

The simulated transducers' faces (i.e., their active front surfaces) were all slightly concave, with a curvature radius of 20 cm and a width of 25 mm. All were placed at a 38° angle to normal incidence, with a distance of 35 mm between the pipe and the lower edge of the

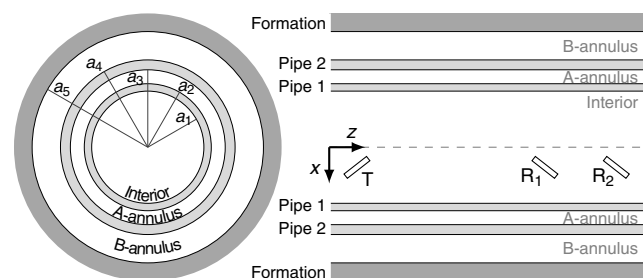


Figure 1. Transverse cross section of double-casing well geometry (left) and sagittal cross section with a pitch-catch setup (right). The lower half of the latter cross section was simulated in this work.

transducer face. This choice of angle corresponds to that of Wang et al. (2014) and Tian et al. (2011). The distance between the face center of the transmitter and that of the near and far receivers was 25 and 35 cm, respectively, giving a distance $\Delta z = 10$ cm between the two receivers.

The coordinate system was chosen as shown to the right in Figure 1, so that z is the coordinate along the well length and x is the coordinate along the well radius, with $x = 0$ being the symmetry axis of pipe 1 and the borehole. The length of the system was chosen as 43 cm, giving a small space on both sides of the pitch-catch setup.

The simulations themselves were performed in the 2D sagittal half-cross section shown to the right in Figure 1. The FEM software COMSOL Multiphysics was used to perform time-domain simulations of the system, solving the wave equation in the fluids and the isotropic linear elastic equations in the solids. COMSOL was developed for such simulations, among others, and has been found to give good results for time-domain simulations of elastic waves by authors such as Hora and Cervená (2012) and McKenna et al. (2008). Our resulting FEM model could be adapted to various permutations of the system geometry and materials, with the materials used listed in Table A-2.

Here, FEM simulations were chosen mainly due to familiarity with the software, and time-domain simulations were chosen to be able to easily follow the measurement pulse in time as it passes through the simulated system. We expect that explicit finite-difference simulations (He et al., 2014) or analytical models (Zeroug, 2000), once implemented, would be significantly faster and less computationally demanding. However, because all these methods solve the same equations in the bulk media, their results would be near-identical.

The transmitter was implemented as a normal acceleration boundary condition on the transducer face, applying an apodized Gaussian pulse

$$\frac{\partial^2 u_n}{\partial t^2} = -B e^{-(t-t_p/2)^2/(2\sigma_t^2)} \sin[2\pi f_0(t-t_p/2)] \sin(s\pi), \quad (2)$$

where u_n is the normal displacement, f_0 is the center frequency, $t_p = 4/f_0$ is the pulse length, $\sigma_t^2 \approx 4.00 \mu s^2$ is the time variance for a Gaussian pulse with a relative bandwidth of 0.75, and s is a spatial parameter that runs from zero to one over the length of the transducer face. Because all the simulated equations are linear, the amplitude B is arbitrary and was chosen as $B = 1 \text{ m/s}^2$. Like He et al. (2014), we have chosen $f_0 = 250 \text{ kHz}$, although our pulse is shorter to be better able to separate different wavefronts. Thus, we use the same combination of frequency and incidence angle as Tian et al. (2011) report for a real tool in a specific logging case. From Zeroug and Froelich (2003), this combination of frequency and incidence angle ensures that the flexural A0 mode is cleanly excited with little contribution from other modes. Because the reflection coefficient curves shown in that paper were made for plane-wave incidence, our wavefronts mandate an extra margin of safety in the choice of frequency and transducer angle. This is because they contain a spectrum of incidence angles as they are emitted from a finite source.

The receivers recorded unfiltered signals $S'_{R_1}(t)$ and $S'_{R_2}(t)$ as a weighted integral of the pressure p over their faces,

$$S'_{R_n}(t) = \int_0^1 p(s, t) \sin(s\pi) ds. \quad (3)$$

To reduce low-frequency fluidborne noise from the transmitter's sidelobes, all signals were subsequently filtered with a zero-phase high-pass filter. The resulting filtered receiver signals $S_{R_1}(t)$ and $S_{R_2}(t)$ were additionally normalized with the maximum of the filtered transmitter signal $S_T(t)$, which was similarly found through a weighted pressure integral. The maxima used for normalization were the peak value of the signal envelope, which was calculated as the absolute value of the analytic signal found through the Hilbert transform. Due to this normalization, the signals $S_{R_n}(t)$ are dimensionless. This is in contrast to some previous publications, (Zeroug, 1998), in which the incident pressure is converted to voltage through a more complex transducer modeling process. Additionally, our transducer surfaces were modeled as acoustically hard boundaries. The reason for this simple approach is that detailed modeling of the transducers' sound reception is not required to study the propagation of the pulse through the system as long as both transducers receive sound in the same way.

Quadratic triangular elements were used with a maximum size of $dx_{\max} = (c_{\text{water}}/f_0)/10$. The time step dt was chosen from Courant number considerations so that $c_{p,\text{steel}}/(dx_{\max}/dt) = 0.4$. To validate that this choice of resolution is sufficient, a higher resolution simulation with $c_{p,\text{steel}}/(dx_{\max}/dt) = 0.2$ and $dx_{\max} = (c_{\text{water}}/f_0)/(10\sqrt{2})$ was performed. Comparing the simulation-measured peaks used later in this paper between the higher resolution and normal-resolution simulations, we find a relative amplitude error of 0.6% or less and an absolute arrival time error of 0.15 μs or less. These low errors indicate that our normal simulation resolution is sufficient.

To minimize spurious reflections, the low-reflecting boundary conditions described in COMSOL (2015a, 2015b) were used on the outer edges of the system. Although these boundaries are noticeably reflective for waves at high incidence angles, these reflections were found to arrive much later than the pulses that were analyzed, and therefore do not affect the analysis. This is discussed further in the "Discussion" section.

SIMULATION RESULTS

The evolution of the transmitted pulse through the system for a case with foam cement in the B-annulus is shown in Figure 2, and the received signals are shown in Figure 3. The generation of the primary wave packet can be clearly seen from Figure 2b to 2c, and in the latter, we see the reflection of the leaked wave off pipe 2. In Figure 2d, we can see the primary and secondary wave packets on pipe 1, and we see the development of corresponding leaky Lamb wave packets on pipe 2. The moments where the receivers are insonified by the pressure pulses leaked by the primary and secondary wave packets — henceforth called the primary and secondary pulses — can be correlated between Figure 2e and 2f and Figure 3.

Inserting $S_{R_{1,1}}$ and $S_{R_{2,1}}$ into equation 1, where $S_{R_{n,i}}$ is the amplitude of the i th Lamb wave-emitted pulse on the n th receiver, gives an attenuation of $\alpha_1 = 0.54 \text{ dB/cm}$ (the same attenuation was found in all simulations where only pipe 2 and/or the B-annulus was changed). Additionally, from the pulse peak arrival times $t_{R_{1,1}}$

and $t_{R_{2,1}}$, we can calculate the group speed of our Lamb wave packets on pipe 1 as

$$c_L = \frac{\Delta z}{t_{R_{2,1}} - t_{R_{1,1}}} \approx 3180 \text{ m/s}. \quad (4)$$

This is in line with the group speed curves shown by Zeroug and Froelich (2003).

The simulations were performed in series. In each series, a small number of parameters were varied between simulations. Each series was performed and analyzed separately.

Series 1: Material variation in B-annulus

For each of the materials listed in Table A-2, a simulation was performed with that material in the B-annulus, and the resulting secondary pulse amplitudes $S_{R_{n,2}}$ were determined. These were used to determine an amplitude ratio of the secondary wave packet measurements, defined analogously to α_1 in equation 1 as

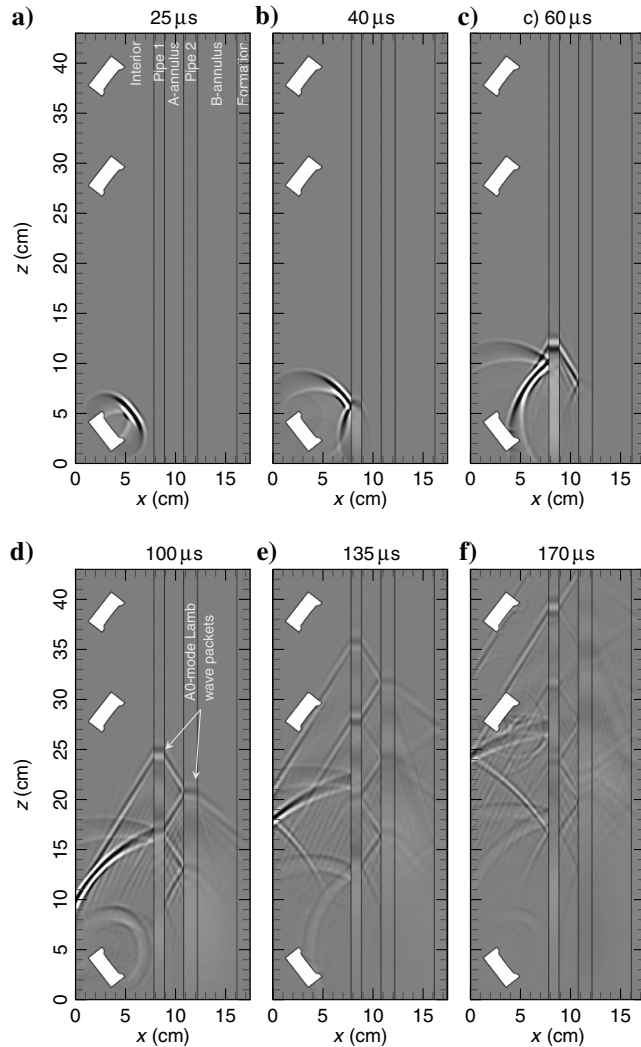


Figure 2. Snapshots of pressure p (interior and A-annulus) and displacement u_x (pipes 1 and 2 and B-annulus) at (a-f) six different points in time, for a simulation with foam cement in the B-annulus.

$$\alpha_2 = \frac{20}{\Delta z} \log_{10} \left(\frac{S_{R_{1,2}}}{S_{R_{2,2}}} \right). \quad (5)$$

The results are shown in Figure 4, where cases of $\alpha_2 < 0$ correspond to $S_{R_{2,2}} > S_{R_{1,2}}$, i.e., the secondary wave packet increasing in amplitude between the two receivers. The figure separates between “slow” and “fast” materials, in which the latter have a P-wave speed such that $c_p > c_L$. The reason for this separation is that the attenuation radically changes its character from slower to faster materials, as shown for a single-frequency time-harmonic case by van Kuijk et al. (2005). For the results of our time-domain wave packet case,

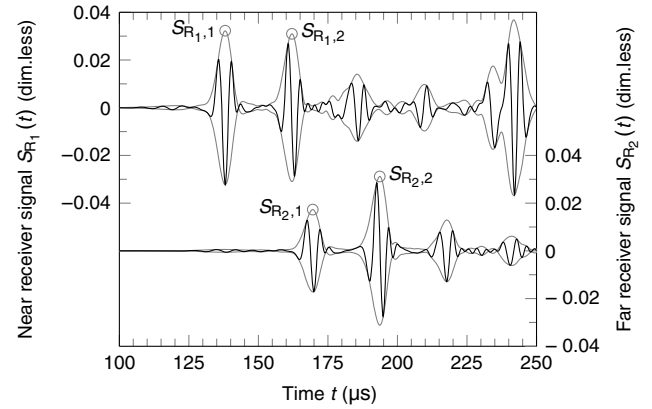


Figure 3. Filtered and normalized signals (black) from both receivers for the case shown in Figure 2. Also shown are the signal envelopes (gray) and the determined peaks (circles).

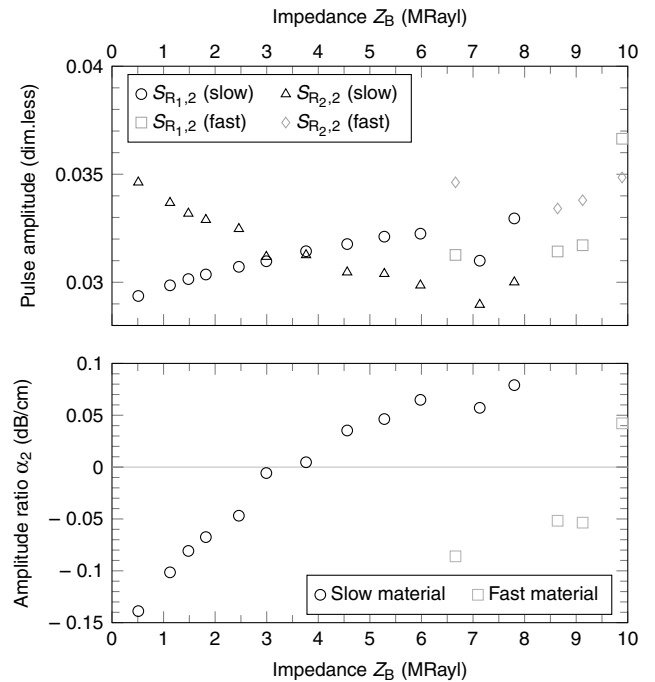


Figure 4. Variation of (a) secondary pulse amplitudes from receivers and (b) amplitude ratio α_2 with variation of material in B-annulus. Slow and fast materials have lower and higher P-wave speeds than $c_L \approx 3180$ m/s, respectively.

we found c_L to be an appropriate separation point between two differently behaved sets of results. This difference comes from a change in the P-wave coupling between the Lamb wave and the adjacent medium: The Lamb wave is “supersonic” compared to a slow medium in which it radiates distinctive wavefronts, whereas it is “subsonic” compared to a fast medium in which P-waves will be absent or evanescent (note that the wave packet will also radiate S-waves into solids as seen in the B-annulus in Figure 2, and these S-waves will be present as long as $c_L > c_s$).

Series 2: Variation in casing standoff

As can be seen from the left part of Figure 1, the radii a_n will depend on the azimuthal angle if the pipes are eccentric. However, if pipe 1 (including the transducers) is eccentric in the plane of the simulated sagittal cross section, the simulation geometry is altered only by a change of the standoff between the two casings, i.e., the A-annulus width $d_A = a_3 - a_2$. A series of simulations were therefore performed for various values of d_A to investigate the effect of such standoff variations (we note, however, that approximating eccentricity by standoff variations neglects any 3D effects due to the curvature of the casings). In each simulation, the interior and annuli contained water.

When examining the results, it was found for very small separation d_A that the primary and secondary pulses arrived so close together that they are nearly indistinguishable, with the lowest resolvable width approximately 0.5 cm for water in the A-annulus. For this reason, these simulations were not analyzed further. The pulse amplitudes and arrival times found in the other simulations are shown in Figure 5.

Series 3: Variation in pipe 2 thickness and B-annulus material

The effect of pipe thickness was examined by performing a run of simulations over five different materials in the B-annulus and three different pipe 2 thicknesses d_{p_2} . These three thicknesses were the original pipe 2 thickness (0.545 in.), the same thickness as pipe 1 (0.408 in.), and an intermediate thickness (0.477 in.). The materials were all chosen as slow materials from Table A-2, with $c_p < c_L$, though their impedances (1.13, 1.48, 2.99, 5.28, and 7.13 MRayl) otherwise cover a large part of the impedance spectrum. The pulse amplitudes and the values of α_2 are shown for all 15 cases in Figure 6.

DISCUSSION

In Figure 2, we see that the transmitted pulse generates a complex train of leaky Lamb wave packets on both pipes. We will now interpret the individual steps leading to this result.

When the pulse from the transducer insonifies pipe 1, it generates the primary flexural Lamb wave packet as seen in Figure 2b. This wave packet leaks distinctive wavefronts into both adjacent media, given that there is wave coupling between the pipe and each medium. As the wavefront into the A-annulus is reflected from pipe 2, it starts setting up a corresponding leaky Lamb wave packet in the outer pipe as seen from Figure 2c to 2d. The leaked wave from the new wave packet on pipe 2 and the reflected wavefront from the primary wave packet together build up the secondary Lamb wave packet on pipe 1.

The overall behavior is that of a cascade between the Lamb wave packets. All later wave packets appear due to the continuous leakage from preceding wave packets; they are not simple reflections of the original incident pressure pulse. This can be seen from Figure 3 in which the primary wave packet decays significantly from the near receiver to the far, whereas the secondary wave packet does not, indicating that the second pulse’s amplitude loss due to leakage is balanced by the amplitude gain from preceding packets. Therefore, applying the term “third interface echo” to the secondary pulse may give the wrong idea because it implies a simple interface reflection.

It should be pointed out that this behavior is dependent on the material in the A-annulus: If the P-wave speed in this material is higher than the Lamb wave speed, the P-wave coupling is broken and wave packets on pipe 1 cannot set up wave packets on pipe 2 in the same way, unless the A-annulus material is a solid so that the two pipes may communicate through shear coupling.

Later in this discussion, we will substantiate these interpretations by building a simple mathematical model based on them. We will subsequently show that this model can match the evolution of the wave packet amplitudes.

In addition to the pulses from the Lamb wave packets, the receivers pick up fluidborne sound from the transmitter. Most clearly, we see the reflected pulse from pipe 1 in Figure 2b–2f. The wave propagates through the fluid and hits receiver R_1 approximately $t = 180 \mu\text{s}$. This can also be seen as noise in $S_{R_1}(t)$ in Figure 3, and the measured peak amplitude $S_{R_1,3}$ should therefore be considered unreliable.

In Figure 2e and 2f, we can also see that this wave is partly reflected off the boundary at $x = 0$. This is an unphysical effect caused by the imperfect nature of the applied boundary condition, which causes waves at high outgoing angles to be reflected back

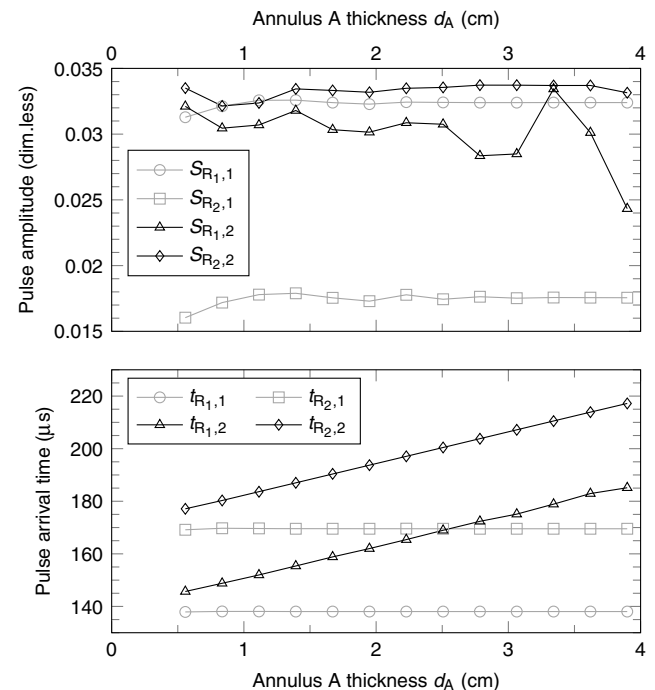


Figure 5. (a) Amplitudes and (b) arrival times for primary and secondary pulses with variation in casing standoff.

into the system. As we can see in Figure 2f, this wave is again reflected off the inner pipe. It hits R_1 approximately $t = 242 \mu\text{s}$, causing a strong pulse in $S_{R_1}(t)$ visible in Figure 3. However, this unphysical pulse arrives much too late to affect any of the peaks $S_{R_{1,i}}$ used in this work.

A third fluidborne wave is the initial pulse's reflection off pipe 1 and the transducer. We can see this wave in Figure 2d–2f. It arrives roughly simultaneously with the previously mentioned unphysical pulse.

Discussion of the simulation series

Series 1: Material variation in B-annulus

Figure 4 shows that when the B-annulus impedance Z_B is varied, the received secondary pulse amplitudes $S_{R_{1,2}}$ and $S_{R_{2,2}}$ clearly vary with it. This shows that the bonding quality on the fourth interface may in principle be detected through the amplitude of the secondary pulse.

For low values of Z_B , we see that $S_{R_{2,2}} > S_{R_{1,2}}$, which means that the Lamb wave packet increases in amplitude because it propagates from one receiver to the next, leading to negative values of α_2 . This behavior is reversed for higher values of Z_B , in which the wave packet decreases in amplitude.

Although $S_{R_{1,2}}$ and $S_{R_{2,2}}$ evolve fairly linearly with impedance for the slow materials, the fast materials break this trend. This change is in accordance with van Kuijk et al. (2005), who show that the Lamb wave attenuation changes drastically from slower to faster materials. In Figure 4, all the fast materials except the

one with the highest impedance show similar behavior, suggesting that their attenuation falls in the high- Z region of slowly varying attenuation $\alpha(Z)$ shown by van Kuijk et al. (2005).

Series 2: Variation in casing standoff

Figure 5 clearly shows that the arrival time of the secondary pulse depends linearly on standoff, though this has already been well-established by Zeroug and Froelich (2003) and van Kuijk et al. (2005). When the two pipes are so close as to be almost touching, it becomes difficult to distinguish the primary and secondary pulses. This might also be the case when control lines in the annulus are nearly touching the pipe, allowing detection of the azimuthal position of these control lines. More interesting is the variation in amplitudes. The primary pulses are fairly constant in amplitude except at small d_A where they interfere with the secondary pulses. Similarly, $S_{R_{2,2}}$ is also fairly constant except for this interference.

However, the amplitude $S_{R_{1,2}}$ varies strongly for large d_A . Looking at the corresponding arrival time, we can see that there is a strong variation approximately $t = 180 \mu\text{s}$, where we have already established that the fluidborne direct sound hits receiver R_1 . Consequently, this strong variation is likely due to interference. As explained by Haldorsen et al. (2006), avoiding such interference between fluidborne waves and formation-path waves is a basic principle of sonic tool design. We see here that this principle must be extended to the secondary Lamb waves when they are to be used in ultrasonics. Even so, the fluidborne waves will be weakened in strongly attenuating muds, possibly diminishing the interference.

Series 3: Variation of pipe 2 thickness and B-annulus material

Figure 6 shows that the effect of varying the pipe 2 thickness can be very significant. For equal pipe thicknesses and low impedances, the results differ strongly from the rest. This can be explained by the dispersion relations on both pipes being very similar in this case. When the dispersion relations are similar, the wave packets on pipe 2 go more slowly out of phase with the incoming leaked waves from pipe 1, so that the interference between the incoming wave and the wave packet becomes more constructive.

Even for unequal pipe thicknesses, we can see that the effect of thickness variation is strong. The effect on pulse amplitudes and α_2 is of similar significance to the effect of Z_B variation shown in Figure 4.

Limited mathematical model

Some of the physical insights gained in this study can be encapsulated and verified as a heuristic mathematical model. The aim of this model is to track the evolution of the wave packets' amplitudes $B_n(t)$ in a double-pipe geometry, as shown in Figure 7. These amplitudes $B_n(t)$ can be found in the simulations as the peak of the envelope of each wave packet's displacement u_x .

The model will be derived under the following limiting assumptions:

- 1) two dimensionality, such as in the simulations presented above
- 2) equal thickness on both pipes and therefore equal dispersion relations, so that wave packets on both remain in the same relative phase
- 3) no external reflecting surfaces such as transducers or a formation

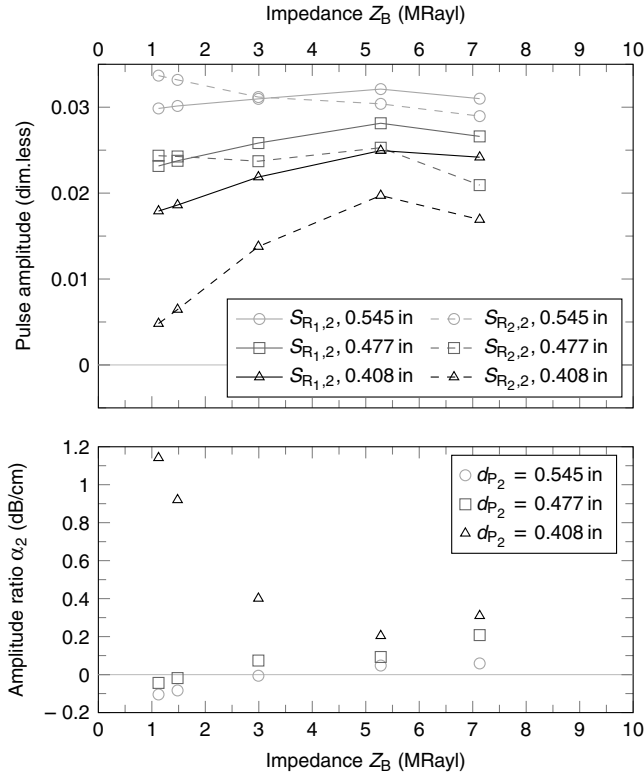


Figure 6. Variation of (a) secondary pulse amplitudes from receivers and (b) amplitude ratio α_2 with variation in the pipe 2 thickness d_{p_2} and the material in the B-annulus.

- 4) the pipes are perfectly parallel
- 5) there is fluid between the pipes, so that they only interact through pressure waves
- 6) all wave packet amplitudes $B_n(t)$ are zero until a simple primary wave packet $B_1(t)$ enters the system at time t_0
- 7) the pipes are far enough apart that individual wave packets remain spatially well-separated.

Derivation

From van Kuijk et al. (2006), we know that the attenuation of a flexural Lamb wave packet is approximately proportional to the sum of the impedances of materials in contact if these materials are slow, i.e.,

$$\alpha_1 \propto Z_I + Z_A, \quad (6)$$

where Z_I , Z_A , and Z_B are the impedances of the interior, the A-annulus, and the B-annulus, respectively. We can show that this behavior can be captured by describing the decay of the primary wave packet $B_1(t)$ through the ordinary differential equation (ODE)

$$\frac{dB_1(t)}{dt} = -(\lambda_I + \lambda_A)B_1(t), \quad (7)$$

where $\lambda_I \propto Z_I$, $\lambda_A \propto Z_A$, and $\lambda_B \propto Z_B$ are decay constants for wave radiation into the interior fluid, the A-annulus, and the B-annulus, respectively. Applying the initial condition that the primary wave packet enters the system at $t = t_0$ with a given amplitude, the solution of this ODE is

$$B_1(t) = B_1(0)e^{-(\lambda_I + \lambda_A)t}H(t - t_0), \quad (8)$$

where $B_1(0)$ is the extrapolated amplitude at $t = 0$ and $H(t)$ is the Heaviside function given by

$$H(t) = \begin{cases} 0 & \text{for } t < 0, \\ 1 & \text{for } t \geq 0. \end{cases} \quad (9)$$

Equation 8 implies that the amplitude decays spatially as $e^{-(\lambda_I + \lambda_A)x/c_L}$, which is consistent with equation 6 because $\lambda_I \propto Z_I$ and $\lambda_A \propto Z_A$. Thus, we have shown that equation 7 captures the behavior of equation 6.

The amplitude leaked from $B_1(t)$ into the A-annulus is proportional to $\lambda_A B_1(t)$. When this leaked wave hits pipe 2, we assume that it is partly transmitted into $B_2(t)$ with a transmission coefficient T . Thus, $B_2(t)$ changes because of two factors: The gain due to the incoming wave and the loss due to the wavefronts leaked into both annuli. Mathematically, this gain is expressed through the time-delayed loss in $B_1(t)$, such that

$$\frac{dB_2(t)}{dt} = T\lambda_A B_1(t - \Delta t) - (\lambda_A + \lambda_B)B_2(t), \quad (10)$$

where Δt is the time-of-flight between adjacent wave packets.

We assume that part of the leaked wave from $B_1(t)$ is also reflected off pipe 2 with a reflection coefficient R . Thus, the secondary Lamb wave amplitude $B_3(t)$ is affected by this reflected wave, the wave leaked from $B_2(t)$, and the loss due to leakage, as

$$\begin{aligned} \frac{dB_3(t)}{dt} = & RT\lambda_A B_1(t - 2\Delta t) \\ & + T\lambda_A B_2(t - \Delta t) - (\lambda_I + \lambda_A)B_3(t). \end{aligned} \quad (11)$$

Higher order reflections come into play for later wave packets. Thus, any wave packet is affected by all preceding wave packets and its own leakage. This can be expressed through the general ODE

$$\frac{dB_n(t)}{dt} = T\lambda_A \sum_{i=1}^{n-1} R^{n-(i+1)} B_i[t - (n-i)\Delta t] - \lambda_n B_n(t), \quad (12)$$

where

$$\lambda_n = \begin{cases} (\lambda_I + \lambda_A) & \text{for } n \text{ odd,} \\ (\lambda_A + \lambda_B) & \text{for } n \text{ even,} \end{cases} \quad (13)$$

is the total decay constant for wave packet n . This model assumes that T and R are the same on both casings, which neglects any effect that the casing curvature might have. However, for the purposes of this paper, this is not an issue as the model will only be applied to a 2D simulation.

Thus, equations 8 and 12 thus model the evolution of all wave packet amplitudes, given the model parameters t_0 , $B_1(0)$, λ_I , λ_A , λ_B , Δt , T , and R . Considerations on the continuity of amplitude suggest a stability criterion $R + T \leq 1$ (there is an inequality rather than an equality here as other Lamb modes may be excited). This suggestion is confirmed by solving the ODE system and seeing that the amplitude sum $\sum_n B_n(t)$ diverges otherwise. Additionally, the amplitude sum oscillates divergently for $T > 2$.

Comparison with stripped simulation

The simulation model presented above was adapted for comparison with this model. The transducers and formation were removed, the thickness of pipe 2 was set equal to that of pipe 1, and the Lamb wave packet was introduced as a time-dependent boundary condition on pipe 1 at $z = 0$, where a displacement pulse $u_x(t)$ was im-

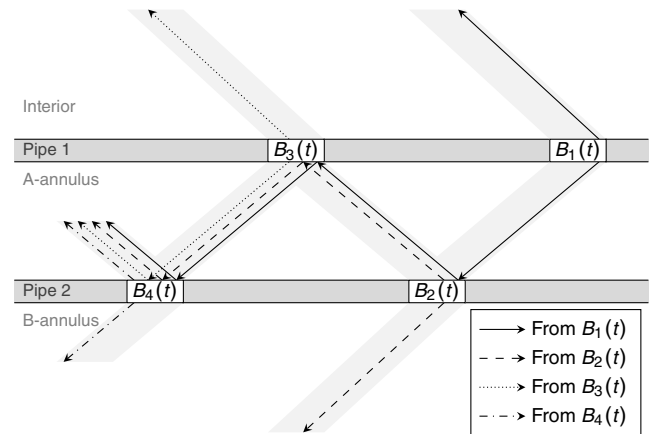


Figure 7. Schematic overview of the interaction between leaky Lamb wave packets on two parallel pipes, as seen in Figure 2e. Arrows show the influence from earlier wave packets on later ones.

posed given by the right side of equation 2. The purpose of this stripped model is to be able to detect the wave packets more clearly; in Figure 2c–2f, significant displacements not related to the wave packets are visible on the pipes.

Two cases were simulated:

- 1) Case 1: The only applied material was water, with $Z_I = Z_A = Z_B = 1.48$ MRayl.
- 2) Case 2: Three different materials from Table A-2 were applied, with $Z_I = 1.13$ MRayl, $Z_A = 1.48$ MRayl, and $Z_B = 2.46$ MRayl.

The evolution of this model for case 1 is shown in Figure 8. Weaker leaked waves from excited A1 Lamb modes can also be seen in front of the wave packets themselves. Similar leaked waves can also be faintly seen in Figure 2, though these are actually from S0 Lamb modes (the different excitation methods in the simulations underlying Figures 2 and 8 cause different modes to be excited). This is also shown but not commented elsewhere in the literature (Zeroug and Froelich, 2003; Wang et al., 2014).

The displacement $u_x(z, t)$ was measured along the centerlines of the two pipes for each microsecond. From the envelopes of $u_x(z, t)$, the time evolution of the wave packet amplitudes was determined by picking the peak value of each wave packet at various time steps. The peak amplitudes $|B_n(t)|$, presented for cases 1 and 2 in Figure 9, were also normalized by the amplitude B of the pulse imposed on the boundary. Noticeable oscillations can be seen in the amplitudes:

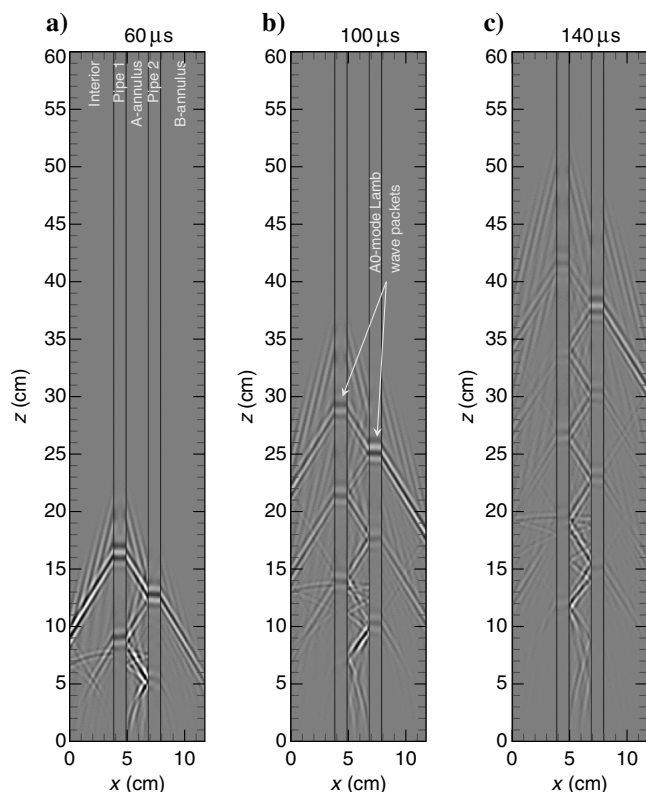


Figure 8. Snapshots of the stripped simulation with water outside and between the pipes, showing pressure p (interior and annulus) and displacement u_x (pipes 1 and 2) at (a–c) three different points in time. The simulation-measured wave packet amplitude evolution is shown in the upper axes of Figure 9.

The peaks exhibited a variation due to background noise (no filtering was applied) and dispersion.

Determining the ODE model parameters such that the resulting modeled amplitudes from equation 12 fit the measured wave packet amplitudes is an optimization problem. This was solved using an unconstrained nonlinear optimization method as described by Lagarias et al. (1998). The optimization objective function was chosen as the root-mean-square value of the difference between the simulated and the modeled amplitudes, discarding areas in which the amplitudes fell below a certain threshold to avoid a perceived noise floor in the measurements $u_x(z, t)$. Thus, the fit between simulated and modeled amplitudes was optimized in a least-squares sense. In case 1, the optimization was constrained so that $\lambda_I = \lambda_A = \lambda_B$.

Figure 9 compares the amplitude evolution measured in each simulation and the corresponding modeled amplitudes found through parameter optimization of the ODE model. The optimized parameters for each case can be found in Table A-3.

The fit between the simulation measurements and the modeled amplitudes is generally very good, showing that there is merit in

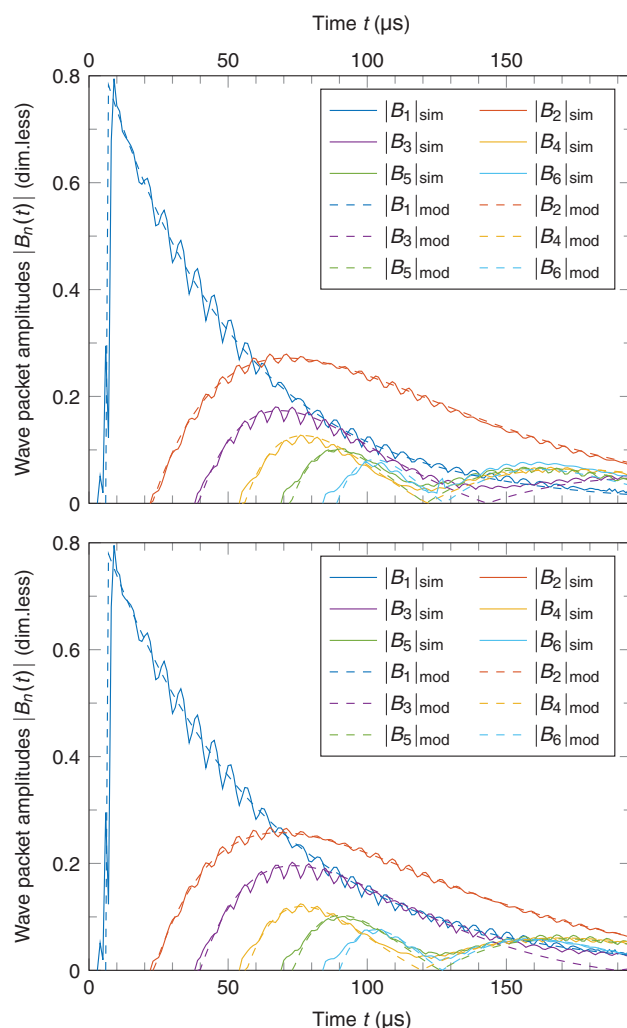


Figure 9. Simulation-measured (solid) and modeled (dashed) amplitude evolution of the six first wave packets for (a) cases 1 and (b) 2. The amplitudes are normalized by that of the imposed displacement boundary condition.

the model. However, we observed that the optimization algorithm can reach somewhat different sets of parameters depending on the initial condition. Although these parameter sets all resulted in similar values of the objective function and a similarly visually good fit, the parameters reported in Table A-3 do not necessarily represent a global optimum.

However, some discrepancies between the two sets of curves are visible. Most obvious is the fact that the modeled values $|B_n(t)|$ go to zero when the wave packet experiences a change in its sign. The simulation-measured $|B_n(t)|$ do not reach zero, and we attribute this to a noise floor on each pipe. In addition, the simulation-measured amplitude $|B_1(t)|$ does not cleanly rise at $t \approx t_0$ because of the peak detection algorithm used.

For both cases, the resulting parameters t_0 , λ_A , Δt , and R were as expected very similar, in addition to the initial pulse amplitude $B_1(t_0)$. The decay constants in case 2 fulfill $\lambda_1/\lambda_A \approx Z_1/Z_A$ and $\lambda_B/\lambda_A \approx Z_B/Z_A$, as could be expected from equations 6 and 7.

The wave packet evolution from this model can be connected with the full model described previously in this paper. For instance, the attenuation α_1 can be found from the decay constants as

$$\alpha_1 = (\lambda_1 + \lambda_A) \frac{20 \log_{10} e}{c_L} = 0.56 \text{ dB/cm}. \quad (14)$$

This is very similar to the value 0.54 dB/cm determined above from $S_{R1,1}$ and $S_{R1,2}$. Because the amplitude at a point on the leaked wavefront is linked to the amplitude of the wave packet when the wavefront point was emitted, we expect that a setup with additional receivers R_n would yield curves of, e.g., $\{S_{Rn,2}\}$ against time similar to the $|B_3(t)|$ curves shown in Figure 9.

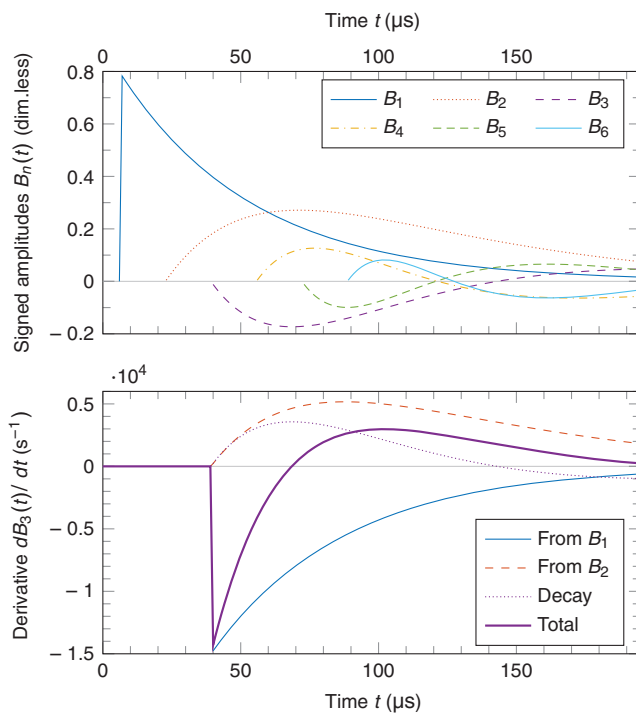


Figure 10. For case 1, the signed modeled wave packet amplitudes showing (a) the zero crossings and (b) the components of the time derivative of $B_3(t)$.

This model may also give some more insight into the evolution of each wave packet. Figure 10 shows the signed wave packet amplitudes $B_n(t)$; the wave packets that are initially of opposite sign are set up through odd numbers of reflections of the leaked wave from the primary wave packet. The figure shows that later wave packets can change their sign as the weight of influence changes from one wave packet to another. From Figure 9, we can see that this also happens in the simulations, taking into account the noise floor that prevents the simulation-measured amplitudes $|B_n(t)|$ from reaching zero.

Figure 10 also shows the influences on the evolution of the secondary wave packet $B_3(t)$, which was the focus of our investigation of the full simulation. At first, the influence from the primary wave packet $B_1(t)$ dominates, but as this packet decays and $B_2(t)$ increases in amplitude, the latter becomes the major influence on $B_3(t)$. This leads us to a possible explanation for the influence on Z_B on $S_{Rn,2}$ as seen in Figures 4 and 6: Increasing Z_B will cause $B_2(t)$ to decay faster, diminishing its influence on $B_3(t)$, from which $S_{Rn,2}$ are measured.

The behavior of the primary wave packet is quite simple: It decays exponentially, and this decay can be measured using as few as two receivers. However, we have seen here that the later wave packets' behavior is more complex, indicating that more receivers would be very useful to draw out information from these packets' evolution.

Although this model gives us some insight into the evolution of wave packets in some particular cases, its limitations as listed above restrict its usefulness. We also attempted to simulate a case with pipes of unequal thickness as shown in Figure 2 using a stripped model as shown in Figure 8, and the resulting simulation-measured packet amplitudes $B_n(t)$ proved impossible to fit with modeled amplitudes like in Figure 9. However, because a difference in pipe thickness gives different flexural propagation speeds in the two pipes, the assumptions underlying the derivation of the ODE system in equation 12 are not valid in this case. Thus, it is unlikely that this explanatory model can be directly applied in practical situations.

CONCLUSIONS

In this work, we used an FEM model of an ultrasonic pitch-catch setup in the double-casing geometry shown in Figure 1 to simulate the propagation of the pulse from the transmitter to the two receivers. In this way, we found that applying existing pitch-catch methods in this geometry results in a train of Lamb wave packets appearing on both casings as shown in Figure 2. We have shown that later-arriving wave packets are not merely caused by reflections of the wave leaked from the primary wave packet, but that there is rather a more complex behavior at play in which later wave packets are affected by all the preceding ones.

We showed in Figure 4 that the B-annulus impedance Z_B affects the amplitude of the secondary wavefront, meaning that the recorded pitch-catch waveforms contain information about the bonding behind the outer casing in through-tubing situations.

Standoff variation of the pipes in our 2D cross section was shown to have a well-behaved effect on the arrival time as shown in Figure 5, though this has already been well-established in the literature. The effect of standoff variations was not strong on the pulse amplitudes, unless the primary and secondary pulses arrived close enough to interfere, or if the secondary pulses arrived simultane-

ously with a fluidborne direct pulse. Given a particular tool design, such considerations may place restrictions on the range of applicability of logging methods based on the secondary pulse. However, only the effect of eccentricity on the casing standoff in a 2D cross section was evaluated here, and the effect of eccentricity is bound to be more complex in three dimensions.

We saw a clear effect on the received pulses when the thickness of the casings was changed, as shown in Figure 6. Thus, it may perhaps also be possible to determine the thickness of the outer casing from such pitch-catch measurements, although this would require being able to separate this effect from that caused by the variation of Z_B . If this is not possible, perhaps it may be possible to measure the outer casing thickness using another approach and use that measurement to compensate.

Some insight into the system's behavior can be gleaned through the mathematical model presented here, which models the time evolution of each wave packet on each pipe. This model shows how the later packets are influenced by the preceding packets' attenuation and leaked wavefronts. However, this model is still quite limited. Notably, the model does not work in cases in which the pipes are of unequal thickness because it assumes equal dispersion properties of both pipes so that the different wave packets preserve their relative phase and interfere perfectly constructively or perfectly destructively. For this mathematical model to be more generally useful, it must be developed further. Still, it does already show us that the evolution of the later packets is more complex than that of the primary packet. This indicates that a tool with more than two receivers would be able to draw more information from the later packets because it would be able to measure the relative wave packet amplitudes at more than two points along their time evolution. The benefits of additional receivers should be investigated in the future works, as well as the benefits of drawing information from even later wave packets.

The through-tubing cases presented here are quite idealized. Future work should consider the effects of material variation in the A-annulus, corroded casings, casings that are not perfectly parallel, and debonding. Additionally, our 2D simulations may miss certain 3D physical effects. Therefore, future work on this topic must also include 3D simulations to support these 2D results. In particular, the effects that eccentricity on the outer casing at various angles relative to the pitch-catch setup can have on the received signals must be studied in detail.

We showed that several effects may affect the measured amplitude of the secondary pulses, and we expect that other effects we did not consider here may be relevant. It remains to be seen how these different effects may be separated to get unambiguous results. Although the work presented here cannot yet be used in practical logging situations, it does indicate that it is possible to log beyond the second casing using ultrasonic pitch-catch tools.

ACKNOWLEDGMENTS

This work has been sponsored by Statoil. We are deeply grateful to D. Miller of Miller Applied Science and J. Haldorsen of READ AS. We acknowledge the aid of Statoil's K. Constable and P. Hemmingsen, and we acknowledge the Statoil summer students R. Sivertsen and S. Vik Furuseth for their dedication and constructive feedback.

APPENDIX A

SIMULATED MATERIAL PARAMETERS

The basic simulation model contained casings of steel and a formation of stone, with material parameters as given in Table A-1. In all cases, the interior and A-annulus contained water.

Different materials were used in our simulations for the material in the B-annulus. Instead of using a smoothly varying artificial continuum of materials as was partly done by van Kuijk et al. (2005), we chose a wide variety of realistic materials to simulate even though many of them would not typically be found in a well annulus. This was done so that the simulated materials had a large spread in properties, to ensure that our results are valid even for widely varying materials. The materials used are shown in Table A-2. However, measurements of the solids' shear speed c_s were not available. Instead, we used an empirical expression from Castagna et al. (1985),

$$c_s = \frac{c_p - 1360 \text{ m/s}}{1.16}. \quad (\text{A-1})$$

Materials where this would lead to a negative shear speed were treated as fluids.

Table A-1. Density ρ , Young's modulus E , and Poisson's ratio ν of basic solids in the model.

Material	ρ (kg/m ³)	E (GPa)	ν
Steel	7850	205	0.28
Sandstone	2200	38.8	0.26

Table A-2. P-wave speed c_p , density ρ , and impedance Z of simulated materials. The five first materials were treated as fluids.

Materials	c_p (m/s)	ρ (kg/m ³)	Z (MRayl)
Scree	300	1700	0.51
Oil	1250	900	1.13
Water	1481	1000	1.48
Mud	1400	1300	1.82
Saturated shales and clays	1200	2050	2.46
Foam cement	2250	1330	2.99
Sat. shales and sand sect.	1750	2150	3.76
Chalk (1)	2400	1900	4.56
Marls	2400	2200	5.28
Porous and saturated sandstone (1)	2600	2300	5.98
Class G cement	3700	1800	6.66
Porous and saturated sandstone (2)	3100	2300	7.13
Chalk (2)	2600	3000	7.80
Limestone	3600	2400	8.64
Dolomite	3650	2500	9.13
Salt	4600	2150	9.89

Table A-3. Optimized model parameters for cases 1 and 2.

Parameter	Case 1	Case 2
$B_1(0)$	9.04	8.82
t_0 (μs)	6.2	6.5
λ_I (s^{-1})	1.03×10^4	0.76×10^4
λ_A (s^{-1})	1.03×10^4	1.01×10^4
λ_B (s^{-1})	1.03×10^4	1.68×10^4
Δt (μs)	16.5	16.7
T	1.85	1.95
R	-0.99	-0.98

REFERENCES

- Arbuzov, A. A., 2012, Memory magnetic imaging defectoscopy: Presented at the SPE Russian Oil and Gas Exploration and Production Technical Conference, 10.
- Bellabarba, M., H. Bulte-Ioyer, B. Froelich, S. Le Roy-Delage, R. van Kuijk, S. Zeroug, D. Guillot, N. Moroni, S. Pastor, and A. Zanchi, 2008, Ensuring zonal isolation beyond the life of the well: Oilfield Review, **20**, 18–31.
- Brill, T. M., C. Demichel, E. A. Nichols, and F. Z. Bermudez, 2011, Electromagnetic casing inspection tool for corrosion evaluation: Presented at the International Petroleum Technology Conference, 14.
- Castagna, J. P., M. L. Batzle, and R. L. Eastwood, 1985, Relationships between compressional-wave in elastic silicate rocks and shear-wave velocities: Geophysics, **50**, 571–581, doi: [10.1190/1.1441933](https://doi.org/10.1190/1.1441933).
- COMSOL, 2015a, Acoustics module user's guide: COMSOL.
- COMSOL, 2015b, Structural mechanics module user's guide: COMSOL.
- Donovan, G., P. Fadesere, G. Ware, L. Daigle, F. Suparman, G. Frisch, P. Fox, M. Englar, G. Moake, and W. Guo, 2015, Behind pipe log evaluation study: Deepwater subsea abandonments in the Gulf of Mexico: Presented at the SPE Annual Technical Conference and Exhibition, 23.
- Haldorsen, J., D. Johnson, T. Plona, B. Sinha, H.-P. Valero, and K. Winkler, 2006, Borehole acoustic waves: Oilfield Review, **18**, no. 1, 34–43.
- Hayman, A., R. Hutin, and P. Wright, 1991, High-resolution cementation and corrosion imaging by ultrasound: Presented at the SPWLA 32nd Annual Logging Symposium.
- He, X., H. Chen, and X. Wang, 2014, Ultrasonic leaky flexural waves in multilayered media: Cement bond detection for cased wellbores: Geophysics, **79**, no. 2, A7–A11, doi: [10.1190/geo2013-0361.1](https://doi.org/10.1190/geo2013-0361.1).
- Hora, P., and O. Cervená, 2012, Determination of Lamb wave dispersion curves by means of Fourier transform: Applied and Computational Mechanics, **6**, 5–16.
- Lagarias, J. C., J. A. Reeds, M. H. Wright, and P. E. Wright, 1998, Convergence properties of the Nelder-Mead simplex method in low dimensions: SIAM Journal of Optimization, **9**, 112–147, doi: [10.1137/S1052623496303470](https://doi.org/10.1137/S1052623496303470).
- McKenna, J., M. McKenna, S. Yushanov, J. Crompton, and K. Koppenhoefer, 2008, Computational modeling of wave propagation in a geophysical domain: Presented at the COMSOL Conference.
- NORSOK D-010, 2013, Well integrity in drilling and well operations (4th ed.): Standards Norway.
- Tian, J., Q. Wang, Q. Guo, H. Guo, and C. Liu, 2011, Casing integrity evaluation in deep well with extreme heavy mud in Tarim Basin: Proceedings of the SPE EUROPEC/EAGE Annual Conference and Exhibition, SPE 140982, 1–8.
- van Kuijk, R., J.-L. le Calvez, and B. Froelich, 2006, Determination of the impedance of a material behind a casing combining two sets of ultrasonic measurements: U.S. Patent 7,149,146 B2.
- van Kuijk, R., S. Zeroug, B. Froelich, M. Allouche, S. Bose, D. Miller, J.-L. le Calvez, V. Schoepf, and A. Pagnin, 2005, A novel ultrasonic cased-hole imager for enhanced cement evaluation: Presented at the International Petroleum Technology Conference.
- Wang, H., G. Tao, X. Shang, and C. Xiao, 2014, Review of acoustic logging on cement bond and studies on acoustic/ultrasonic methods for low-density cement bond logging: Well Logging Technology, **38**, 165–173.
- Wright, P., 1993, Method and apparatus for the acoustic investigation of a casing cemented in a borehole: U.S. Patent 5,216,638.
- Zeroug, S., 1998, Spectral integral formulae for the response of acoustic transducers in cylindrically curved configurations: IEEE Transactions on Ultrasonics, Ferroelectrics, and Frequency Control, **45**, 768–778, doi: [10.1109/58.677727](https://doi.org/10.1109/58.677727).
- Zeroug, S., 2000, Analytical modeling for fast simulations of ultrasonic measurements on fluid-loaded layered elastic structures: IEEE Transactions on Ultrasonics, Ferroelectrics, and Frequency Control, **47**, 565–574, doi: [10.1109/58.842043](https://doi.org/10.1109/58.842043).
- Zeroug, S., 2002, Method and apparatus for ultrasonic imaging of a cased well: U.S. Patent 6,483,777 B1.
- Zeroug, S., and B. Froelich, 2003, Ultrasonic leaky-Lamb wave imaging through a highly contrasting layer: Proceedings of the IEEE Symposium on Ultrasonics, 794–798.

This article has been cited by:

1. Hua Wang, Michael Fehler. 2018. The wavefield of acoustic logging in a cased-hole with a single casing – Part I: a monopole tool. *Geophysical Journal International* **212**:1, 612-626. [[Crossref](#)]
2. Erlend Magnus Viggen, Tonni Franke Johansen, Ioan-Alexandru Merciu. 2017. Simulation and inversion of ultrasonic pitch-catch through-tubing well logging with an array of receivers. *NDT & E International* **85**, 72-75. [[Crossref](#)]
3. Jakob B. U. Haldorsen, Espen Stensrud, Ioan-Alexandru Merciu, Douglas E. Miller. 2016. Characterizing borehole plumbing using full-waveform ultrasonic data: Application to data from a North Sea well. *GEOPHYSICS* **81**:6, B189-B199. [[Abstract](#)] [[Full Text](#)] [[PDF](#)] [[PDF w/Links](#)]
4. Erlend Magnus Viggen, Tonni Franke Johansen, Ioan-Alexandru Merciu. 2016. Analysis of outer-casing echoes in simulations of ultrasonic pulse-echo through-tubing logging. *GEOPHYSICS* **81**:6, D679-D685. [[Abstract](#)] [[Full Text](#)] [[PDF](#)] [[PDF w/Links](#)]